Supporting Information for

Ultrafast Dynamics and Liquid Structure in Mesoporous Silica: Propagation of Surface Effects in a Polar Aprotic Solvent

Samantha T. Hung,[†] Steven A. Yamada,[†] Weizhong Zheng,[‡**] and Michael D. Fayer[†*]

[†]Department of Chemistry
Stanford University, Stanford, CA 94305, USA
*Phone: (650) 723-4446; Email: fayer@stanford.edu

[‡]State Key Laboratory of Chemical Engineering
East China University of Science and Technology, Shanghai 200237, China
**Phone: (021) 64253175; Email: wzzheng@ecust.edu.cn

1. Simulation Details

The silica pore models used in the MD simulations were constructed by carving cylindrical pores (2.8, 5.4, and 8.3 nm diameters) out of amorphous silica blocks. Dangling-bond O and Si atoms on the surfaces of the cylindrical pores were correspondingly saturated with H and OH groups to generate surface silanol groups. The resulting surface silanol density was 4.8 ± 0.3 sites/nm^2, which is in good agreement with the experimental value of 4.9 ± 0.5 sites/nm^2.[1] The cell dimensions of the 2.8, 5.4, and 8.3 nm silica pore models are 4.28×4.28×4.40, 7.55×7.55×4.40, and 11.20×11.20×4.40 nm^3, respectively. Bulk MeIm boxes with the same dimensions were built using Packmol.[2] To obtain model pores filled with MeIm molecules, the silica pore models were sandwiched between two corresponding bulk MeIm boxes along the axial direction of the cylindrical pores (the *z* axis). This sandwich-like assembly was the starting point for the MD simulations. First, non-optimal geometrical configurations were eliminated through 5000 steps of energy minimization. The resultant boxes were then equilibrated under the canonical (*NVT*) ensemble with a Berendsen thermostat at 296.2 K for 40 ns to fully fill the pores. MeIm molecules located outside the silica framework were removed, leaving 183, 721, and 1742 confined MeIm molecules in the 2.8, 5.4, and 8.3 nm models, respectively. To match the molar ratio of $SeCN^-$ (vibrational probe) to MeIm (1:200) used in experimental conditions, 1, 3, and 9 MeIm molecules at the pore center were replaced with corresponding numbers of BmimSeCN ion pairs in the 2.8, 5.4, and 8.3 nm models, respectively. The resulting model of confined MeIm and BmimSeCN for a 5.4 nm pore is shown in Fig. S1. The composite boxes were further equilibrated for 20 ns under the *NVT* ensemble with a Nose-Hoover thermostat at

296.2 K and run for an additional 60 ns to obtain the properties of interest.

The interactions between the silica, MeIm, and BmimSeCN were represented by Lennard-Jones (L-J) interactions. The L-J parameters of the silica model had been validated in our previous works.[3-4] The parameters for MeIm and BmimSeCN were taken from the OPLS-AA force field. All of the MD simulations were conducted using GROMACS with 1 fs time steps.[5-8] Lorentz-Berthelot mixing rules were employed with periodic boundary conditions in three dimensions. During the simulations, the silica framework was fixed, but the angles and dihedral angles of the Si-OH and $Si(OH)_2$ groups on the pore surface were flexible. The Si-O and O-H bond lengths of the Si-OH and $Si(OH)_2$ groups were fixed at 1.54 and 0.98 Å, respectively. The particle mesh Ewald method with a cut-off radius of 1.2 nm was used to treat the long-range electrostatic interactions. The initial velocities were randomly generated from a Maxwell-Boltzmann distribution. The LINCS algorithm was used to constrain the covalent bonds including hydrogen atoms.

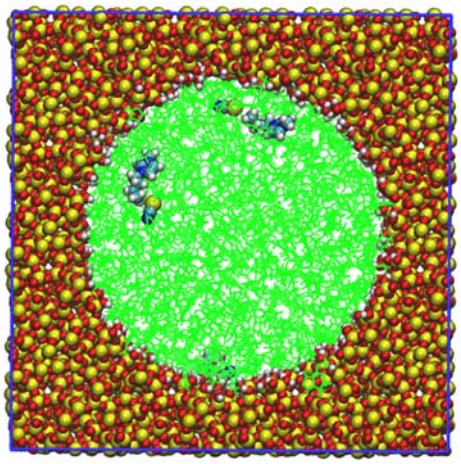

Figure S1. Cross-sectional view of MD simulation snapshots of MeIm (green) and BmimSeCN (van der Waals models) confined in a 5.4 nm silica pore model.

2. Hydrogen Bonding and the Linear Absorption Spectra

Hydrogen bonding (H-bonding) interactions are important to the solvatochromism of $SeCN^-$. Stronger H-bonds to the $SeCN^-$ nitrogen atom produces a blue shift, due to the increase in the CN triple bond character, which has a bluer frequency than a double bond character CN. H-bonding to the nitrogen end of CN shortens (and strengthens) the CN bond since the molecular orbitals of both the CN and the H-bond donor are delocalized throughout the adduct.[9] In contrast,

stronger H-bonds to the OD deuterium in HOD water weaken the covalent OD bond, leading to a redshift in the OD stretch frequency.[10] This is why confinement resulted in opposite spectral shifts in water confined in AOT reversed micelles (RMs) when studied with $SeCN^-$ versus HOD. In RMs with anionic head groups, increasing confinement increases the population of probes interacting with the anion surface groups relative to those interacting with water.[11] The strength of H-bonds the probe forms increases in the order of: no interactions, interactions with anions, and interactions with water. Since the average strength of probe H-bonds formed are weaker with increasing confinement, the center frequencies of the OD spectrum blue shifts[11] and the $SeCN^-$ spectrum redshifts[12].

H-bonding between $SeCN^-$ and MeIm are influenced by the interactions of MeIm with the silica pore surface. For imidazole (structural analog of MeIm), the compact region of high electron density on the sp^2 hybridized lone pair on the N3 atom (numbering scheme in main text, Fig. 1) facilitates H-bond formation, and charge transfer through the σ electron system and concurrent π electron polarization leaves the N3 atom more negatively charged and the N1 hydrogen atom more H-bond donating.[13] H-bonds between the N3 atom on MeIm and the surface silanols may similarly make the ring hydrogens on MeIm more H-bond donating. Different silanol groups have varying adsorption and H-bond donating properties,[14-15] and can change the properties of the interacting MeIm, and subsequently the $SeCN^-$ vibrational frequency, to varying extents. For bulk MeIm, H-bonds with $SeCN^-$ are present but low in number, and formed mostly via the MeIm C2 hydrogen.[8] Stronger H-bonds formed via these C2 hydrogens may result in a blue shift of the $SeCN^-$ spectrum. H-bonds between $SeCN^-$ and the C4 and C5 hydrogens that may previously be absent may become possible; these may be weaker and redder. Increases in both contributions may explain the broadening of the $SeCN^-$ linewidth without a clear shift in center frequency.

The vibrational frequency of $SeCN^-$ is also influenced by the number and orientation of the H-bonds it forms. Categorization of H-bonds to $SeCN^-$ in D_2O revealed that H-bonds roughly collinear with the CN bond (axial type) are stronger and hence blue shifted, while weaker, off-axis H-bonds (equatorial type, typically forming where an axial bonds is already present) are redshifted.[16] This dependence of the CN frequency with the angle of H-bonds had been observed in other studies of protic solvents as well.[17-18] Molecular orbital calculations similarly showed that two H-bonds to the nitrogen end of $SeCN^-$ produce a redshift relative to a single interaction.[9]

Simulations of $SeCN^-$ in D_2O confined in silica pores revealed a slight inhibition of H-bond formation under confinement, decreasing the total number of H-bonds, but not the axial population.[19] While the confined D_2O spectra were surprisingly similar to the bulk in terms of band center and width, the red wing in the bulk spectrum is noticeably reduced in the confined spectra.[19-20] The red wing was attributed to the non-Condon effect,[16, 21] or the frequency dependence of the transition dipole strength, with weaker transition dipoles being assigned to bluer frequency CN's and stronger transition dipoles to those with redder frequencies, resulting in higher absorbance on the red side of the spectrum. Thus, the diminished contribution of the redder equatorial H-bonds in the pores led to a diminished red wing.

A similar reduction in the red wing was also observed in confined MeIm, though the red wing in the bulk spectrum is small to begin with, as seen by extending a Voigt fit of the bluer side of the spectra to the full range of the absorption band (Fig. S2). The reduced red wing suggests that the relative proportion of bluer H-bonds increased with confinement. One explanation is that MeIm becomes more H-bond donating upon confinement and thus capable of forming stronger and thus bluer H-bonds with $SeCN^-$. However, the center frequency was unchanged. Another explanation is a steric argument that the electrostatic ordering of MeIm to the surface reduced the probability of $SeCN^-$ forming additional equatorial (red) H-bonds to other MeIm molecules after forming an axial H-bond with one MeIm molecule. Detailed simulations can help clarify both the reduction of the red wing and the broader line shape by determining the types and relative ratios of H-bonds in bulk and confined MeIm.

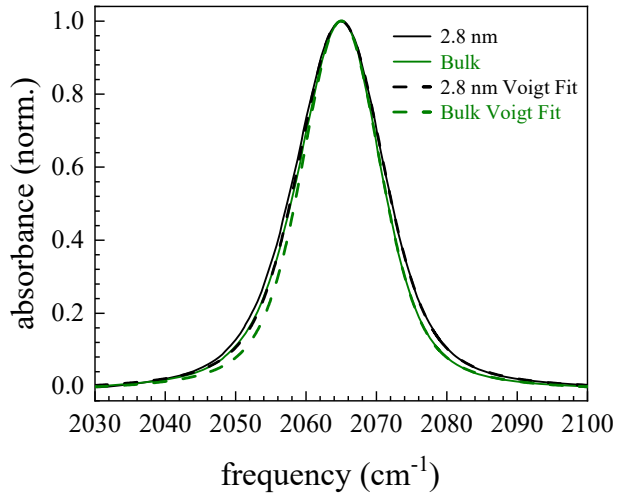

Figure S2. Linear IR spectra of the $SeCN^-$ CN stretch in bulk MeIm (solid green curve) and MeIm confined in 2.8 nm pores (solid black curve). Voigt fits (dashed curves) to the blue sides and peaks of the spectra are extended across the full frequency range, revealing a red wing in the bulk that is diminished in the pore.

3. Isotropic Pump-Probe Signals *P*(*t*)

A. Non-Condon Effect

The non-Condon effect is described by redder $SeCN^-$ oscillators having larger transition dipoles. Thus, even with uniform pumping of the line, more absorption occurs on the red side, resulting in an excited state distribution skewed towards the red. Thermal equilibrium is restored by means of spectral diffusion: as oscillators sample different frequencies via solvent structural fluctuations, a net population transfer across the absorption line occurs, from the red to the blue.[16, 22] The time scales preceding the dominant, slow exponential decay in the *P*(*t*) is comparable to those of spectral diffusion. When these fast time scales were shared across frequencies, their amplitudes decrease with increasing frequency. The positive (negative) amplitudes on the red (blue) side of the absorption line correspond to fast decays (growths), showing a net transfer of population from the red to the blue.

Since the amplitudes of the fast spectral diffusion time scales are small (<5% of the total amplitude), when the *P*(*t*) decays were fit starting at >100 ps, single exponential fits gave the same vibrational lifetimes as multi-exponential fits (Fig. S3) over the entire time range. The non-Condon effect was more subtle in the pore *P*(*t*) decays, consistent with the reduction of the red wing in the pore linear spectra. Hence, fitting the pore decays with a single exponential over the entire time range gave very reasonable fits, with vibrational lifetimes that were within error of the multi-exponential fits.

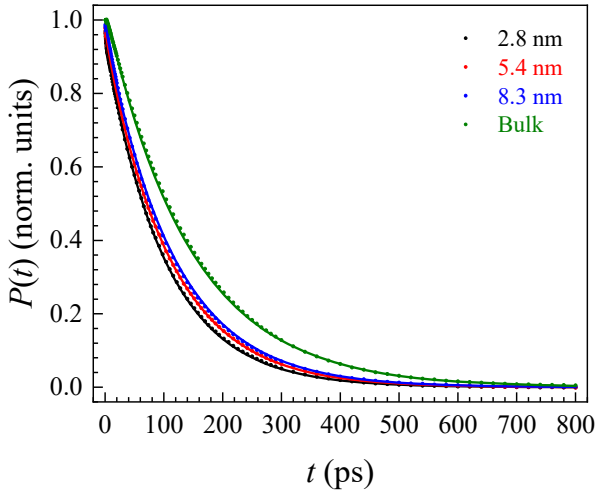

Figure S3. Isotropic pump-probe signal decays near the band center (2065 cm^{-1}) in bulk MeIm (green points) and MeIm confined in silica pores of sizes 8.3 nm (blue points), 5.4 nm (red points), and 2.8 nm (black points). The final time constant of the multi-exponential fits (solid curves) correspond to the $SeCN^-$ CN stretch vibrational lifetimes.

B. Heating Signals (Confined MeIm)

Isotropic heating signals can result in long time offsets, which were observed in the pore $P(t)$. However, fitting $P(t)$ data with small offsets gave identical lifetimes to more involved procedures such as scaled subtraction of the measured non-resonant background signal (on pore samples filled with only MeIm),[23] analytic modeling of probe heat signals,[24] and pulse-shaping of the "pump on" and "pump off" shots to match the heat deposition between shots and hence intrinsically mitigate the non-resonant signal.[25] Likewise, the anisotropy data that were treated using the abovementioned methods also produced fit parameters within error of untreated data. Thus, while these heating signals can be observed, their effects are negligible.

4. Anisotropy Decays $r(t)$

A. Probe Concentration Dependence (Bulk MeIm)

The time constants for the $SeCN^-$ dynamics in bulk MeIm with $Bmim^+$ as the counter ion are faster than those previously reported with K^+ as the counter ion.[8] The KSeCN measured dynamics had been fit to a triexponential with no offset. When the $r(t)$ for 1-800, 1-400, and 1-100 molar concentrations of KSeCN to MeIm were fit to triexponentials with small offsets (Fig. S4), the time constants are the same, but the offsets increase with probe concentration. These time constants are the same as those obtained for 1-200 BmimSeCN to MeIm fit to a triexponential with no offset.

The low amplitude offset was also observed when KSeCN was used to measure rotational dynamics in an imidazolium based ionic liquid (IL).[7] The large positive charge density on the K^+ cation was believed to engender local structuring that locks up the structure of the IL. The small fraction of $SeCN^-$ in these more rigid solvent regions exhibit substantially slower dynamics, while the remainder of the $SeCN^-$ in the unaffected regions reflects the faster, unmodified IL dynamics. This small fraction of slower dynamics showed up as a low amplitude offset that increased with increasing K^+ concentration. Allowing for this offset, the predominant rotational dynamics were unchanged for various KSeCN concentrations.

The K^+ effect affected dynamics in MeIm to a lesser extent, with the largest offset being ~2% of the total amplitude as opposed to ~8% in the IL. The lower susceptibility of MeIm to electrostatic ordering by the K^+ may be related to its neutral charge, compared to the ion pairs in the IL. The lack of an offset when using BmimSeCN confirms that the $Bmim^+$ cation, with its

singly positive charge spread over many more atoms and similarity in structure with MeIm, is unlikely to cause structural ordering. BmimSeCN can be safely used at concentrations giving reasonable signal without altering the underlying dynamics.

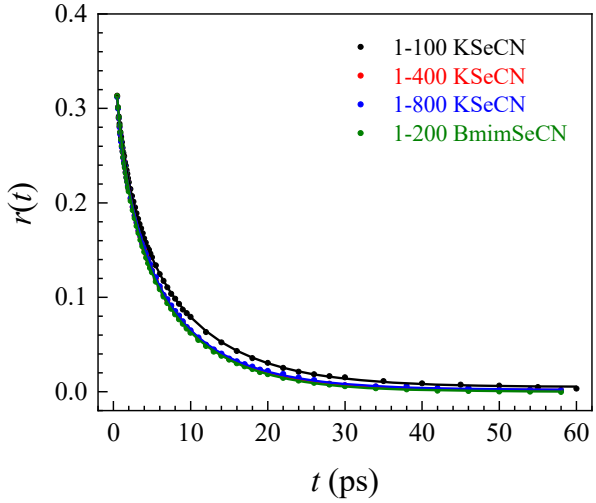

Figure S4. Measured rotational anisotropy $r(t)$ decays of $SeCN^-$ in bulk MeIm (points) for four samples with the $SeCN^-$ added as KSeCN in decreasing molar ratios (1-100, 1-400, 1-800) and as BmimSeCN (1-200 molar ratio). The solid curves are triexponential fits to the data, with the offset fixed to zero only for the BmimSeCN sample. Other than an increase in offset with increasing concentration (most obvious for 1-100 KSeCN), the dynamics are the same.

B. Hydrodynamic Theory

In general, hydrodynamic theory applies best when solute-solvent coupling is purely mechanical, the case for medium sized, spherical solute molecules (hundreds of $Å^3$) rotating in a structureless solvent continuum.[26-28] The theory proposes that the orientational relaxation time τ_m is proportional to the volume V of the rotator (solute) and the bulk dynamic viscosity η of the solvent, and inversely proportional to the absolute temperature T:

$$\tau_m = \frac{\eta V}{k_B T}. \tag{S1}$$

Here, k_B is the Boltzmann constant and for the basic Stokes-Einstein-Debye (SED) model, the rotator is assumed to be a sphere with $V = \frac{4\pi r^3}{3}$.

For the two limiting cases of hydrodynamic theory, stick and slip boundary conditions, the correction factors f (shape or Perrin factor) and C (interaction or boundary condition factor) are multiplied to the right hand side of Eq. S1. The shape factor accounts for deviations from

sphericity of the solute (the value increases from unity with increasing deviation). The boundary condition factor ranges from 0 to 1 depending on solute-solvent interactions. [29-30] For a spherical rotator under stick boundary conditions, $f = 1$ and $C = 1$, and hence the corrected equation reduces to Eq. S1.

One might expect $SeCN^-$ in MeIm to exhibit stick boundary conditions ($C = 1$) since the molecules are comparable in size, and so a $SeCN^-$ molecule will likely drag surrounding MeIm molecules along as it rotates. Under this assumption, without accounting for the shape factor and lower and upper bounds on V from previous studies,[7-8] for η = 1.72 cP, T = 294.7611 K, τ_m ranges from 15 to 28 ps, which is two to three times larger than the experimentally obtained value of 8.4 ps. Rotation in dipolar aprotic solvents such as acetonitrile are often better reproduced by slip boundary conditions,[31-32] which are typically invoked when the solute is small relative to the solvent (or solvent structure), such as in ILs.[7] Modeling $SeCN^-$ as a prolate spheroid instead of a perfect sphere, the total correction factor ($f \cdot C$) takes on the values of 0.19 and 1.29 for slip and stick boundary conditions, respectively.[6-8] Using the upper bound volume, this would give a τ_m of approximately 5.3 ps for the slip boundary condition. This value is shorter but comparable to the experimentally measured value of 8.4 ps. One may expect to further correct this theoretical value due to H-bonding interactions between $SeCN^-$ and MeIm, which would increase resistance to rotation (i.e., dielectric friction) and hence increase the theoretical τ_m towards the experimental value.

5. Spectral Diffusion

A. RISD and Spectral Diffusion

Under circumstances where reorientation-induced spectral diffusion (RISD) occurs, the perpendicular and parallel CLS curves decay over distinctly different time scales. For $SeCN^-$ in bulk MeIm, the differences between the parallel and perpendicular CLS decays are very small (Fig. S5).[8] RISD was thus not considered and only the 2D spectra acquired in the scatter-reducing perpendicular configuration were used for spectral diffusion analysis.

If RISD had been significant, spectral diffusion would proceed through both the structural fluctuations of the solvent (structural spectral diffusion SSD) and rotation of the probe molecule (RISD). RISD typically occurs when the electric field from the surrounding

environment varies on a time scale similar to the probe rotation, and is caused by the first-order Stark effect for a probe molecule with a permanent dipole moment (e.g., $SeCN^-$).[33-35] In general, the slower the SSD relative to rotation, the more significant RISD effects are. RISD accelerates the FFCF decay, giving deceptively fast structural diffusion time scales.

Although orientational relaxation occurs relatively quickly for bulk MeIm, more than half of the amplitude is in the final free diffusion time scale of 8.4 ps (main text, Table II), whereas the majority of the amplitude of the CLS decay is in the first time constant, which is a much shorter time 1.63 ps (main text, Table IV). Furthermore, the dominant term in RISD is $C_1(t)$, the first order orientational correlation function, which is a factor of 3 slower than $C_2(t)$ if both can be modeled with a single exponential. Hence, RISD effects should be very small, and they were.

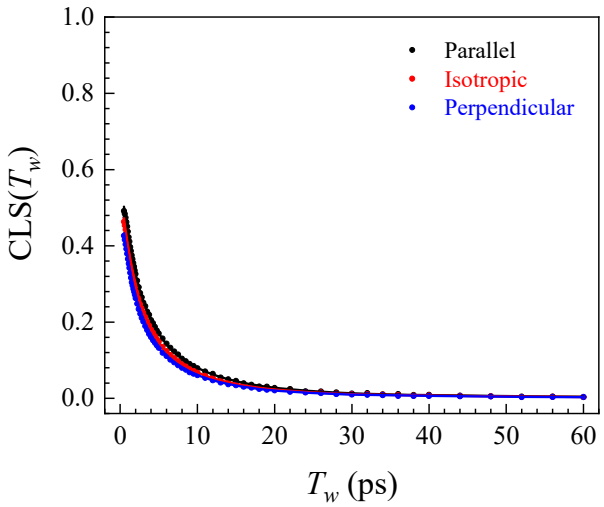

Figure S5. Parallel, isotropic, and perpendicular CLS decays (spectral diffusion) for the CN stretch of $SeCN^-$ in bulk MeIm. The solid curves are triexponential fits to the data.

B. FFCF Parameters

FFCF components can be separated into homogeneous and inhomogeneous contributions. The homogeneous component is a result of motionally narrowed dynamics, the vibrational lifetime, and orientational relaxation. A component is motionally narrowed if $\Delta_i \times \tau_i \ll 1$ (Δ_i in angular frequency units) and inhomogeneously broadened if $\Delta_i \times \tau_i \gg 1$.[36] For a motionally narrowed component, Δ and τ cannot be independently determined. This contribution to the absorption spectrum has a pure dephasing linewidth given by $\Gamma^* = \Delta^2 \tau / \pi = 1/\pi T_2^*$, where T_2^* is

the pure dephasing time. The observed total homogeneous dephasing time T_2 is given by

$$\frac{1}{T_2} = \frac{1}{T_2^*} + \frac{1}{2T_1} + \frac{1}{3T_{or}}, \tag{S2}$$

where T_1 is the vibrational lifetime and T_{or} is the orientational relaxation time.[37] The corresponding homogeneous (Lorentzian) linewidth is $\Gamma = 1/\pi T_2$. For bulk MeIm, the total homogeneous linewidth of ~4 cm^{-1} (main text, Table V) is dominated by motionally narrowed pure dephasing, as the lifetime T_1 (~0.04 cm^{-1}) and orientational relaxation T_{or} (~0.4 cm^{-1}) combined contribute <0.5 cm^{-1}. The inhomogeneous contribution to the absorption spectrum is the convolution of the Gaussian components with standard deviations Δ_i, giving a total inhomogeneous linewidth $\mathrm{FWHM} = 2(2\ln 2)^{1/2}\Delta_{total}$, where $\Delta_{total} = (\sum_i \Delta_i^2)^{1/2}$. The total linear absorption line shape depends on both the Δ_i's and the τ_i's and can be obtained from the FFCF using standard diagrammatic perturbation theory.[38-39] The homogeneous component, 3.5-3.6 cm^{-1} (main text, Table V), is unchanged upon confinement within experimental error. However, its relative contribution to the total line shape decreases with confinement as reflected by the higher initial CLS(T_w) value in the pores (main text, Fig. 5).

6. Simulation Results

A. Simulated Anisotropies *r*(*t*)

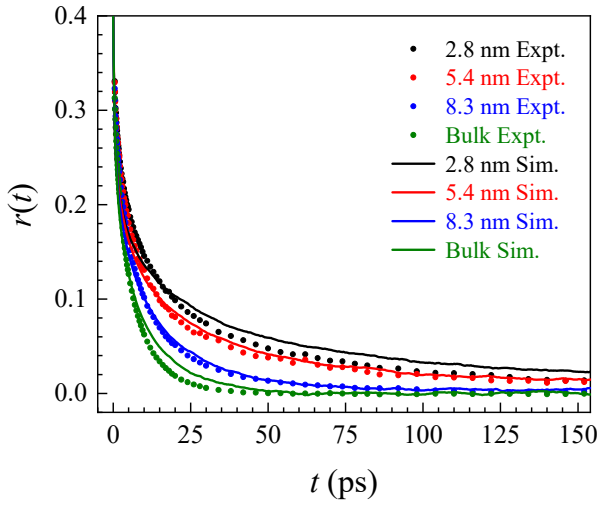

Figure S6. Measured rotational anisotropy $r(t)$ decays of $SeCN^-$ in bulk MeIm (green points) and in MeIm confined in silica pores of sizes 8.3 nm (blue points), 5.4 nm (red points), and 2.8 nm (black points) are compared to the simulated $r(t)$ (solid curves of the same color).

B. Defining the Interfacial Layer

It can be difficult to define an interfacial layer, especially if interdigitated structures exist, such as in acetonitrile, in which case considering two sublayers collectively as the surface layer may be more reasonable.[40] The molecular diameter of MeIm obtained from the Connolly volume is 5.02 Å (main text, Sec. III. B. 1). The corresponding values are 4.11 Å for acetonitrile and 2.70 Å for water. While the precise definition varies across studies, the values obtained from a range of experimental and computational studies on acetonitrile[41-44] and water[20, 45-47] at silica surfaces are usually on the order of one to two molecular diameters. Extracting the layer thickness from the MeIm probability distribution $f(d)$ (Fig. S7) is complicated by the choice of the reference atom for the distance determination and also the orientational preferences of the molecules. We previously determined $\Delta = 4.6$ Å for MeIm as the value of d at the first minimum in the $f(d)$ distribution.[3] However, it can be seen from studies of acetonitrile[41] and water[20] that such values can vary by 1-2 Å depending on which atom on the molecule is used as the reference point. The distance between probability peaks may seem more reliable, but the peak spacing can be influenced by the orientation of the molecules, especially if they are not random. The $f(d)$ peak to peak distance for MeIm is ~2 Å, which is significantly smaller than either 5.02 Å or 4.6 Å. The peak to peak distance for MeIm density, a more general property than the position of specific atoms, is ~4.6 Å, which is consistent with both the Connolly sphere diameter and the $f(d)$ value (first minimum). Considering that the Connolly sphere diameters are comparable to surface thicknesses determined for acetonitrile and water, $\Delta = 4.6$ Å is a reasonable reference value for the MeIm layer thickness.

C. Average Orientational Probability

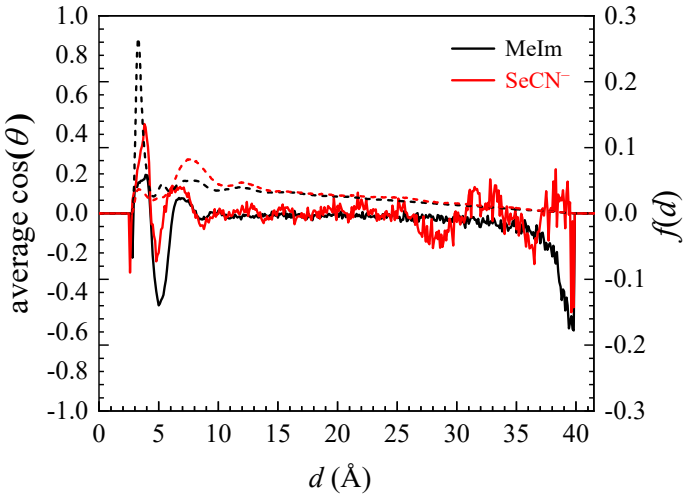

Figure S7. The solid curves are the average orientations of MeIm (black) and $SeCN^-$ (red) as a function of the distance d from the pore surface in an 8.3 nm pore. The colored dashed lines are the corresponding probability distributions, $f(d)$, of the two species (also shown in main text, Fig. 6).

D. Probability Distributions

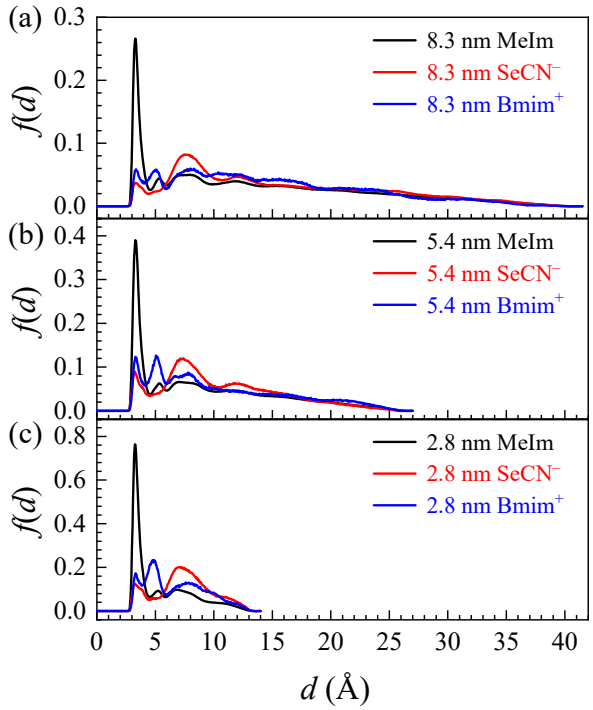

Figure S8. Normalized probability distribution for the MeIm C2 atom (black), $SeCN^-$ carbon atom (red), and $Bmim^+$ C2 atom (blue) as a function of the distance d from the pore surface in (a) 8.3 nm, (b) 5.4 nm, and (c) 2.8 nm pores.

7. Two-State Models

A. Simple Two-State Model Fits

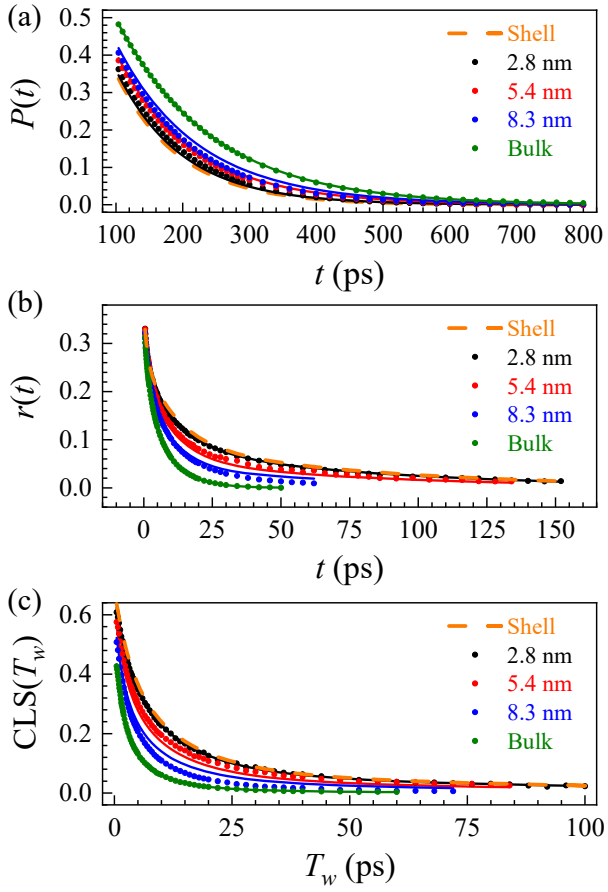

Figure S9. Measured (a) isotropic pump-probe signal decays $P(t)$, (b) rotational anisotropies $r(t)$, and (c) CLS(T_w) decays (spectral diffusion) of $SeCN^-$ in bulk MeIm (green points) and MeIm confined in silica pores of sizes 8.3 nm (blue points), 5.4 nm (red points), and 2.8 nm (black points). The solid curves of the same colors are strict two-state model fits to the data, with an interfacial thickness $\Delta \sim 10.4$ Å. The orange dashed curves are the shell decays that yield the best fit to the experimental data for the three pore sizes.

B. Lifetime Correction

To account for the non-negligible lifetime variation of $SeCN^-$ located at different distances, Eq. 12 (main text) was modified for modeling of the $r(t)$ and the CLS(T_w) by replacing th position-dependent probability distribution $f(\rho)$ of $SeCN^-$ with a version $F(t;\rho)$ that is also time-dependent:

$$F(t;\rho) = f(\rho)\left[1+\left\{\left(e^{-t/\tau_{\text{shell}}}/e^{-t/\tau_{\text{bulk}}}\right)-1\right\}\times m_{\text{lifetime}}(\rho)\right]. \quad \text{(S3)}$$

The quantities τ_{shell} and τ_{bulk} are the vibrational lifetimes tabulated in Table VI (main text) for the shell and core, respectively. The implication of a distance dependent lifetime is that at long time,

the relative contribution of the shell population (with shorter lifetime) to the signal will be reduced.

At long time, the reduction of the shell $SeCN^-$ contribution (with shorter vibrational lifetime) to the signal is mathematically equivalent to a reduction of $SeCN^-$ probability at the surface. Eq. S3 redistributes the $SeCN^-$ probability based on core-shell designations in the original $f(\rho)$ for each time *t*, and thus takes on a form reminiscent of Eq. 11 in the main text. Since the lifetime is longest at the core, the core component is represented by an amplitude 1, and the relative amplitude of signal emitted in the shell region at a given time *t* is represented by the fraction $e^{-t/\tau_{\text{shell}}} / e^{-t/\tau_{\text{bulk}}} \leq 1$.

At time $t = 0$, before any signal decay, no distinction is made between $SeCN^-$ in different MeIm layers. Accordingly, $e^{-t/\tau_{\text{shell}}} / e^{-t/\tau_{\text{bulk}}} = 1$, and Eq. S3 reduces to $F(t;\rho) = f(\rho)$. The long time limit is not meaningful since all signals (shell and core) decay to zero. At an intermediate time *t*, the value of $f(\rho)$ at a given distance ρ is scaled by two factors to give $F(t;\rho)$. The first is the model $m_{\text{lifetime}}(\rho)$, which is the smoothed step function used for modeling the lifetime (main text, Eq. 13), and is thus fit simultaneously to the same parameters in the global fit of all the data sets. This $m_{\text{lifetime}}(\rho)$ term determines the proportion of shell character (lifetime) that a $SeCN^-$ molecule has at distance ρ, and the corresponding fraction of the $f(\rho)$ amplitude at that distance is scaled down by the $e^{-t/\tau_{\text{shell}}} / e^{-t/\tau_{\text{bulk}}}$ term (i.e., the second factor) for the given *t*.

C. Translational Diffusion

If molecules exchange between liquid layers sufficiently fast over the time scale of $SeCN^-$ vibrational relaxation, the measured lifetime at a given distance from the surface would actually be an average of lifetimes of molecules in adjacent liquid layers. If that were the case, the transition from core to shell lifetime may be a simple step function, but manifests as a smoothed step due to spatial translations of the confined species. We will present justifications for why the effects of exchange between core and shell populations in the MeIm system are negligible and thus support the validity of the smoothed step model.

In general, exchange between the core and shell populations should be considered when the time scales of exchange are faster than the dynamics being measured. In computational[41, 43] and OKE[48] studies of acetonitrile rotational dynamics ($C_1(t)$ and collective rotational dynamics)

where an exchange model was invoked, the confined dynamics were dramatically slower than the bulk, taking on different functional forms and decaying to nonzero plateaus. This was not observed for the rotational dynamics ($C_2(t)$) in our MeIm study.

In one of the computational studies of acetonitrile reorientation, the exchange model was attempted since a simple two-state fit to 2.4 nm pore data was poor, although the fits improved with increasing shell thickness.[43] Arbitrarily increasing the shell population to the upper limit of the entire pore population is certainly not a reliable approach, as pore data can always be exactly matched without necessarily reflecting the true dynamics. This is why in the present study, we measured multiple pore sizes to better constrain the fits. Given the decent fits obtained without incorporating exchange, it seems prudent to avoid introducing additional uncertainty associated with including additional fit parameters to describe the exchange equilibrium. In the acetonitrile study, some ambiguity accompanied the use of the exchange model, as a single shell thickness could not be determined, with excellent fits for a range of thicknesses (4-7 Å).[43]

Most importantly, the expected rates of diffusion in the MeIm pores are slow enough that exchange is unlikely to factor significantly. A simple approximation for the bulk MeIm translational diffusion constant D_t can be determined from the Stokes-Einstein law $D_t = \frac{k_B T}{6\pi\eta r}$, which would suggest that the D_t for MeIm should be smaller than acetontrile given their similar size (radii r) and larger (~4x) MeIm viscosity η.[49] Although these liquids may not fulfill the assumptions underlying the Stokes-Einstein law, for both $SeCN^-$ and MeIm in bulk MeIm, the calculated $D_t = 5\times10^{-10}\ \mathrm{m^2/s}$ is the same order of magnitude as binary diffusion coefficients of MeIm obtained via NMR measurements in DMSO ($6.1\times10^{-10}\ \mathrm{m^2/s}$)[50] and in acetonitrile ($7.2\times10^{-10}\ \mathrm{m^2/s}$)[51], and an order of magnitude smaller than $D_t \sim 5\times10^{-9}\ \mathrm{m^2/s}$ for bulk acetonitrile[41]. One study suggested that the slower diffusion of MeIm may be a result of π stacking of the rings.[51]

For a one dimensional random walk, the root mean square (RMS) displacement is given by $\left\langle x^2(t)\right\rangle = 2D_t t$, which is ~1 Å in 10 ps and ~3 Å in 100 ps for bulk MeIm.[52] Under confinement, diffusion tends to be anisotropic due to geometric constraints, and diffusion perpendicular to the surface is often dramatically slower than the bulk, due to energetic and entropic barriers.[53] Diffusion coefficients may not provide appropriate descriptions of the

complex and often subdiffusive behavior of confined liquids, but are useful for quantifying the extent of the slowdown. In a computational study of MeIm confined in 2.8 nm silica, both parallel and perpendicular diffusion coefficients were reduced by an order of magnitude relative to the bulk[4] and in an NMR diffusometry study of pyridine, another nitrogen heterocycle, confined in 3.3 nm silica pores, the perpendicular diffusion coefficient was found to be reduced by two orders of magnitude.[54] An order of magnitude reduction in the diffusion constant corresponds to RMS displacements of ~0.3 Å in 10 ps and ~1 Å in 100 ps.

With the longest shell time scales (for both $r(t)$ and CLS, main text Table VI) being less than 100 ps and the longest core time scales on the order of 10 ps, the corresponding RMS displacements of ~1 Å and ~0.3 Å are well within the error of the model fit parameters (characteristic distances) obtained. Even the upper bound of 3 Å RMS displacement is small, and calculations showed that the smoothed step model for the lifetime cannot be obtained if we start from a strict (or even less "smooth") step model, even with unreasonably large translational displacements (>10 Å in ~140 ps). Considering the small RMS displacements taking place over the time scales of the MeIm dynamics being measured, the effects of shell and core population exchange of both the $SeCN^-$ probe and the MeIm molecules themselves should be negligible and will not be considered. Two-state models without exchange had also been successfully applied to experimental[20] and computational[55] studies of confined water dynamics.

References

1. Zhuravlev, L. T. The Surface Chemistry of Amorphous Silica. Zhuravlev Model. *Colloids Surf. A Physicochem. Eng. Asp.* **2000,** *173* 1-38.
2. Martinez, L.; Andrade, R.; Birgin, E. G.; Martinez, J. M. PACKMOL: A Package for Building Initial Configurations for Molecular Dynamics Simulations. *J. Comput. Chem.* **2009,** *30* 2157-2164.
3. Zheng, W.; Yamada, S. A.; Hung, S. T.; Sun, W.; Zhao, L.; Fayer, M. D. Enhanced Menshutkin S_N2 Reactivity in Mesoporous Silica: The Influence of Surface Catalysis and Confinement. *J. Am. Chem. Soc.* **2020,** *142* 5636-5648.
4. Zheng, W.; Zhao, L.; Sun, W.; Qian, F. Understanding the Confinement Effects and Dynamics of Methylimidazole in Nanoscale Silica Pores. *J. Phys. Chem. C* **2021,** 7421-7430.
5. Lindahl, E.; Hess, B.; Van Der Spoel, D. GROMACS 3.0: A Package for Molecular Simulation and Trajectory Analysis. *Molecular modeling annual* **2001,** *7* 306-317.
6. Bailey, H. E.; Wang, Y.-L.; Fayer, M. D. Impact of Hydrogen Bonding on the Dynamics and Structure of Protic Ionic Liquid/Water Binary Mixtures. *J. Phys. Chem. B* **2017,** *121* 8564-8576.
7. Tamimi, A.; Fayer, M. D. Ionic Liquid Dynamics Measured with 2D IR and IR Pump–Probe Experiments on a Linear Anion and the Influence of Potassium Cations. *J. Phys. Chem. B* **2016,** *120* 5842-5854.
8. Shin, J. Y.; Wang, Y.-L.; Yamada, S. A.; Hung, S. T.; Fayer, M. D. Imidazole and 1-Methylimidazole Hydrogen Bonding and Nonhydrogen Bonding Liquid Dynamics: Ultrafast IR Experiments. *J. Phys. Chem. B* **2019,** *123* 2094-2105.
9. Schultz, P. W. Ab Initio Calculations of Ionic and Hydrogen Bonding Interactions with the OCN^-, SCN^- and $SeCN^-$ Anions. *Mol. Phys.* **1996,** *88* 217-246.
10. Bakker, H. J.; Skinner, J. L. Vibrational Spectroscopy as a Probe of Structure and Dynamics in Liquid Water. *Chem. Rev.* **2010,** *110* 1498-1517.
11. Pieniazek, P. A.; Lin, Y. S.; Chowdhary, J.; Ladanyi, B. M.; Skinner, J. L. Vibrational Spectroscopy and Dynamics of Water Confined inside Reverse Micelles. *J. Phys. Chem. B* **2009,** *113* 15017-15028.
12. Yuan, R.; Yan, C.; Nishida, J.; Fayer, M. D. Dynamics in a Water Interfacial Boundary Layer Investigated with IR Polarization Selective Pump-Probe Experiments. *J. Phys. Chem. B* **2017,**

121 4530-4537.

13. Del Bene, J. E.; Cohen, I. Molecular Orbital Theory of the Hydrogen Bond. 20. Pyrrole and Imidazole as Proton Donors and Proton Acceptors. *J. Am. Chem. Soc.* **1978,** *100* 5285-5290.
14. Edge, M.; Turner, D.; Liauw, C. M.; Robinson, J.; Allen, N. S. The Retention of Heterocyclics by Siliceous Frameworks Part I the Role of the Heterocyclic. *J. Mater. Sci.* **2001,** *36* 1443-1450.
15. Liu, D.; Ma, G.; Allen, H. C. Adsorption of 4-Picoline and Piperidine to the Hydrated SiO_2 Surface: Probing the Surface Acidity with Vibrational Sum Frequency Generation Spectroscopy. *Environ. Sci. Technol* **2005,** *39* 2025-2032.
16. Yamada, S. A.; Thompson, W. H.; Fayer, M. D. Water-Anion Hydrogen Bonding Dynamics: Ultrafast IR Experiments and Simulations. *J. Chem. Phys.* **2017,** *146* 234501.
17. Kim, H.; Cho, M. Infrared Probes for Studying the Structure and Dynamics of Biomolecules. *Chem. Rev.* **2013,** *113* 5817-5847.
18. van Wilderen, L. J. G. W.; Kern-Michler, D.; Müller-Werkmeister, H. M.; Bredenbeck, J. Vibrational Dynamics and Solvatochromism of the Label SCN in Various Solvents and Hemoglobin by Time Dependent IR and 2D-IR Spectroscopy. *Phys. Chem. Chem. Phys.* **2014,** *16* 19643-19653.
19. Yamada, S. A.; Shin, J. Y.; Thompson, W. H.; Fayer, M. D. Water Dynamics in Nanoporous Silica: Ultrafast Vibrational Spectroscopy and Molecular Dynamics Simulations. *J. Phys. Chem. C* **2019,** *123* 5790-5803.
20. Yamada, S. A.; Hung, S. T.; Thompson, W. H.; Fayer, M. D. Effects of Pore Size on Water Dynamics in Mesoporous Silica. *J. Chem. Phys.* **2020,** *152* 154704.
21. Yuan, R.; Yan, C.; Tamimi, A.; Fayer, M. D. Molecular Anion Hydrogen Bonding Dynamics in Aqueous Solution. *J. Phys. Chem. B* **2015,** *119* 13407-13415.
22. Kramer, P. L.; Giammanco, C. H.; Fayer, M. D. Dynamics of Water, Methanol, and Ethanol in a Room Temperature Ionic Liquid. *J. Chem. Phys.* **2015,** *142* 212408.
23. Yuan, R.; Yan, C.; Fayer, M. Ion–Molecule Complex Dissociation and Formation Dynamics in LiCl Aqueous Solutions from 2D IR Spectroscopy. *J. Phys. Chem. B* **2018,** *122* 10582-10592.
24. Rezus, Y. L. A.; Bakker, H. J. On the Orientational Relaxation of HDO in Liquid Water. *J. Chem. Phys.* **2005,** *123* 114502.
25. Hoffman, D. J.; Fica-Contreras, S. M.; Pan, J.; Fayer, M. D. Pulse-Shaped Chopping:

Eliminating and Characterizing Heat Effects in Ultrafast Infrared Spectroscopy. *J. Chem. Phys.* **2020,** *153* 204201.

26. Inamdar, S. R., Rotational Dynamics of Nonpolar and Dipolar Molecules in Polar and Binary Solvent Mixtures. In *Hydrodynamics: Advanced Topics*, Schulz, H.; Simoes, A.; Lobosco, R., Eds. InTech: Rijeka, Croatia, 2011; pp 185-226.
27. Das, S. K.; Sahu, P. K.; Sarkar, M. Diffusion–Viscosity Decoupling in Solute Rotation and Solvent Relaxation of Coumarin153 in Ionic Liquids Containing Fluoroalkylphosphate (FAP) Anion: A Thermophysical and Photophysical Study. *J. Phys. Chem. B* **2013,** *117* 636-647.
28. Turton, D. A.; Wynne, K. Stokes–Einstein–Debye Failure in Molecular Orientational Diffusion: Exception or Rule? *J. Phys. Chem. B* **2014,** *118* 4600-4604.
29. Perrin, F. Mouvement Brownien d'un Ellipsoide-I. Dispersion Diélectrique pour des Molécules Ellipsoidales. *J. Phys. Radium* **1934,** *5* 497-511.
30. Hu, C. M.; Zwanzig, R. Rotational Friction Coefficients for Spheroids with the Slipping Boundary Condition. *J. Chem. Phys.* **1974,** *60* 4354-4357.
31. Morresi, A.; Sassi, P.; Ombelli, M.; Paliani, G.; Cataliotti, R. Rotational Dynamics in Liquid Acetonitrile. Temperature and Concentration Effects in the Non-Ideal CH_3CN/CCl_4 Mixture. *Phys. Chem. Chem. Phys.* **2000,** *2* 2857-2861.
32. Stoppa, A.; Nazet, A.; Buchner, R.; Thoman, A.; Walther, M. Dielectric Response and Collective Dynamics of Acetonitrile. *J. Mol. Liq.* **2015,** *212* 963-968.
33. Kramer, P. L.; Nishida, J.; Giammanco, C. H.; Tamimi, A.; Fayer, M. D. Observation and Theory of Reorientation-Induced Spectral Diffusion in Polarization-Selective 2D IR Spectroscopy. *J. Chem. Phys.* **2015,** *142* 184505.
34. Kramer, P. L.; Nishida, J.; Fayer, M. D. Separation of Experimental 2D IR Frequency-Frequency Correlation Functions into Structural and Reorientation-Induced Contributions. *J. Chem. Phys.* **2015,** *143* 124505.
35. Giammanco, C. H.; Kramer, P. L.; Yamada, S. A.; Nishida, J.; Tamimi, A.; Fayer, M. D. Carbon Dioxide in an Ionic Liquid: Structural and Rotational Dynamics. *J. Chem. Phys.* **2016,** *144* 104506.
36. Hamm, P.; Zanni, M. T., *Concepts and Methods of 2D Infrared Spectroscopy*. Cambridge University Press: New York, 2011.
37. Kwak, K.; Park, S.; Finkelstein, I. J.; Fayer, M. D. Frequency-Frequency Correlation Functions

and Apodization in Two-Dimensional Infrared Vibrational Echo Spectroscopy: A New Approach. *J. Chem. Phys.* **2007,** *127* 124503.

38. Mukamel, S., *Principles of Nonlinear Optical Spectroscopy*. Oxford University Press: Oxford, U.K., 1995.
39. Hoffman, D. J.; Fayer, M. D. CLS Next Gen: Accurate Frequency–Frequency Correlation Functions from Center Line Slope Analysis of 2D Correlation Spectra Using Artificial Neural Networks. *J. Phys. Chem. A* **2020,** *124* 5979-5992.
40. Morales, C. M.; Thompson, W. H. Simulations of Infrared Spectra of Nanoconfined Liquids: Acetonitrile Confined in Nanoscale, Hydrophilic Silica Pores. *J. Phys. Chem. A* **2009,** *113* 1922-1933.
41. Cheng, L.; Morrone, J. A.; Berne, B. J. Structure and Dynamics of Acetonitrile Confined in a Silica Nanopore. *J. Phys. Chem. C* **2012,** *116* 9582-9593.
42. Zhang, J.; Jonas, J. NMR Study of the Geometric Confinement Effects on the Anisotropic Rotational Diffusion of Acetonitrile-d3. *J. Phys. Chem.* **1993,** *97* 8812.
43. Norton, C. D.; Thompson, W. H. Reorientation Dynamics of Nanoconfined Acetonitrile: A Critical Examination of Two-State Models. *J. Phys. Chem. B* **2014,** *118* 8227-8235.
44. Loughnane, B. J.; Farrer, R. A.; Scodinu, A.; Fourkas, J. T. Dynamics of a Wetting Liquid in Nanopores: An Optical Kerr Effect Study of the Dynamics of Acetonitrile Confined in Sol-Gel Glasses. *J. Chem. Phys.* **1999,** *111* 5116-5123.
45. Hagymassy Jr, J.; Brunauer, S.; Mikhail, R. S. Pore Structure Analysis by Water Vapor Adsorption: I. *t*-curves for Water Vapor. *J. Colloid Interface Sci.* **1969,** *29* 485-491.
46. Israelachvili, J. N.; Pashley, R. M. Molecular Layering of Water at Surfaces and Origin of Repulsive Hydration Forces. *Nature* **1983,** *306* 249-250.
47. Bourg, I. C.; Steefel, C. I. Molecular Dynamics Simulations of Water Structure and Diffusion in Silica Nanopores. *J. Phys. Chem. C* **2012,** *116* 11556-11564.
48. Loughnane, B. J.; Scodinu, A.; Fourkas, J. T. Extremely Slow Dynamics of a Weakly Wetting Liquid at a Solid/Liquid Interface: CS_2 Confined in Nanoporous Glasses. *J. Phys. Chem. B* **1999,** *103* 6061-6068.
49. Li, C.; Wang, Y.; Pielak, G. J. Translational and Rotational Diffusion of a Small Globular Protein under Crowded Conditions. *J. Phys. Chem. B* **2009,** *113* 13390-13392.
50. Schleicher, J. C.; Scurto, A. M. Kinetics and Solvent Effects in the Synthesis of Ionic Liquids:

Imidazolium. *Green Chem.* **2009,** *11* 694-703.

51. Schleicher, J. C. Kinetics and Solvent Effects in the Synthesis of Ionic Liquids. Master Thesis, University of Kansas, Lawrence, KS, 2009.
52. Berg, H. C., Diffusion: Microscopic Theory. In *Random Walks in Biology*, Princeton University Press: Princeton, 1984; pp 5-16.
53. Thompson, W. H. Perspective: Dynamics of Confined Liquids. *J. Chem. Phys.* **2018,** *149* 170901.
54. Gedat, E.; Schreiber, A.; Findenegg, G.; Shenderovich, I.; Limbach, H. H.; Buntkowsky, G. Stray Field Gradient NMR Reveals Effects of Hydrogen Bonding on Diffusion Coefficients of Pyridine in Mesoporous Silica. *Magn. Reson. Chem.* **2001,** *39* S149-S157.
55. Laage, D.; Thompson, W. H. Reorientation Dynamics of Nanoconfined Water: Power-Law Decay, Hydrogen-Bond Jumps, and Test of a Two-State Model. *J. Chem. Phys.* **2012,** *136* 044513.